nature photonics

Supplementary information

https://doi.org/10.1038/s41566-025-01779-x

Perturbation-resilient integer arithmetic using optical skyrmions

In the format provided by the authors and unedited

Supplementary Information
Perturbation-resilient integer arithmetic using optical skyrmions

An Aloysius Wang[1,*], Yifei Ma[1], Yunqi Zhang[1], Zimo Zhao[1], Yuxi Cai[1], Xuke Qiu[1], Bowei Dong[2], and Chao He[1,*]

[1]Department of Engineering Science, University of Oxford, Parks Road, Oxford, OX1 3PJ, UK
[2]Institute of Microelectronics (IME), Agency for Science, Technology and Research (A*STAR), 2 Fusionopolis Way, Innovis #08-02, Singapore 138634, Republic of Singapore
[*]Corresponding authors: aloysius.wang@gmail.com, chao.he@eng.ox.ac.uk

1 Experimental design and results

In this section, we describe our experiments in more detail, splitting the discussion into two main parts: beam generation and analysis.

The beam generation technique employed here follows from [1, 2] and consists of two spatial light modulators (SLMs) aligned at a 45° angle to each other (Supplementary Fig. 1). The key mathematical insight is that by parametrizing the Poincaré sphere using spherical coordinates, one has the decomposition

$$\begin{pmatrix} s_1 \\ s_2 \\ s_3 \end{pmatrix} = \begin{pmatrix} \sin\theta\sin\phi \\ \cos\theta \\ \sin\theta\cos\phi \end{pmatrix} = \underbrace{\begin{pmatrix} \cos\phi & 0 & \sin\phi \\ 0 & 1 & 0 \\ -\sin\phi & 0 & \cos\phi \end{pmatrix} \begin{pmatrix} 1 & 0 & 0 \\ 0 & \cos\theta & -\sin\theta \\ 0 & \sin\theta & \cos\theta \end{pmatrix}}_{\text{LC-SLM aligned at } 45^\circ \text{ to each other}} \begin{pmatrix} 0 \\ 1 \\ 0 \end{pmatrix},$$

so that incident 45° linearly polarized light on the SLM cascade can be transformed to any other state of polarization (SoP). In our experiments, the incident Stokes field is a standard Néel-type skyrmion with a beam width of 4mm corresponding to 200×200 pixels on the SLM.

To determine the Stokes field, a rotating quarter-wave plate Stokes polarimeter, as described by Azzam [3], is adopted. This is one of the most widely used configurations today, and consists of a rotating quarter-wave plate and a fixed horizontal polarizer. The quarter-wave plate rotates at a constant speed, modulating the state of polarization of the measurement channel. The resulting intensity variations are captured by a camera, enabling the calculation of the Stokes vector of the light [4]. In our experiments, a calibration method based on Fourier analysis [5] is employed to correct initial azimuth angle errors in the setup, which has been shown to significantly enhance the accuracy of the measured results.

Mueller matrices are measured using a dual-rotating retarder Mueller matrix polarimeter. This system consists of a polarization state generator and a polarization state analyzer [6], each formed with a rotating quarter-wave plate and a horizontal polarizer. The state of polarization in the measurement channels is determined by the specific rotation speed ratio of the two quarter-wave plates, which has been optimized to minimize noise propagation during measurement [7]. Calibration of the dual-rotating retarder Mueller matrix polarimeter also relies on Fourier analysis to correct the initial systematic errors in its configuration [8].

1.1 Experiment assembly

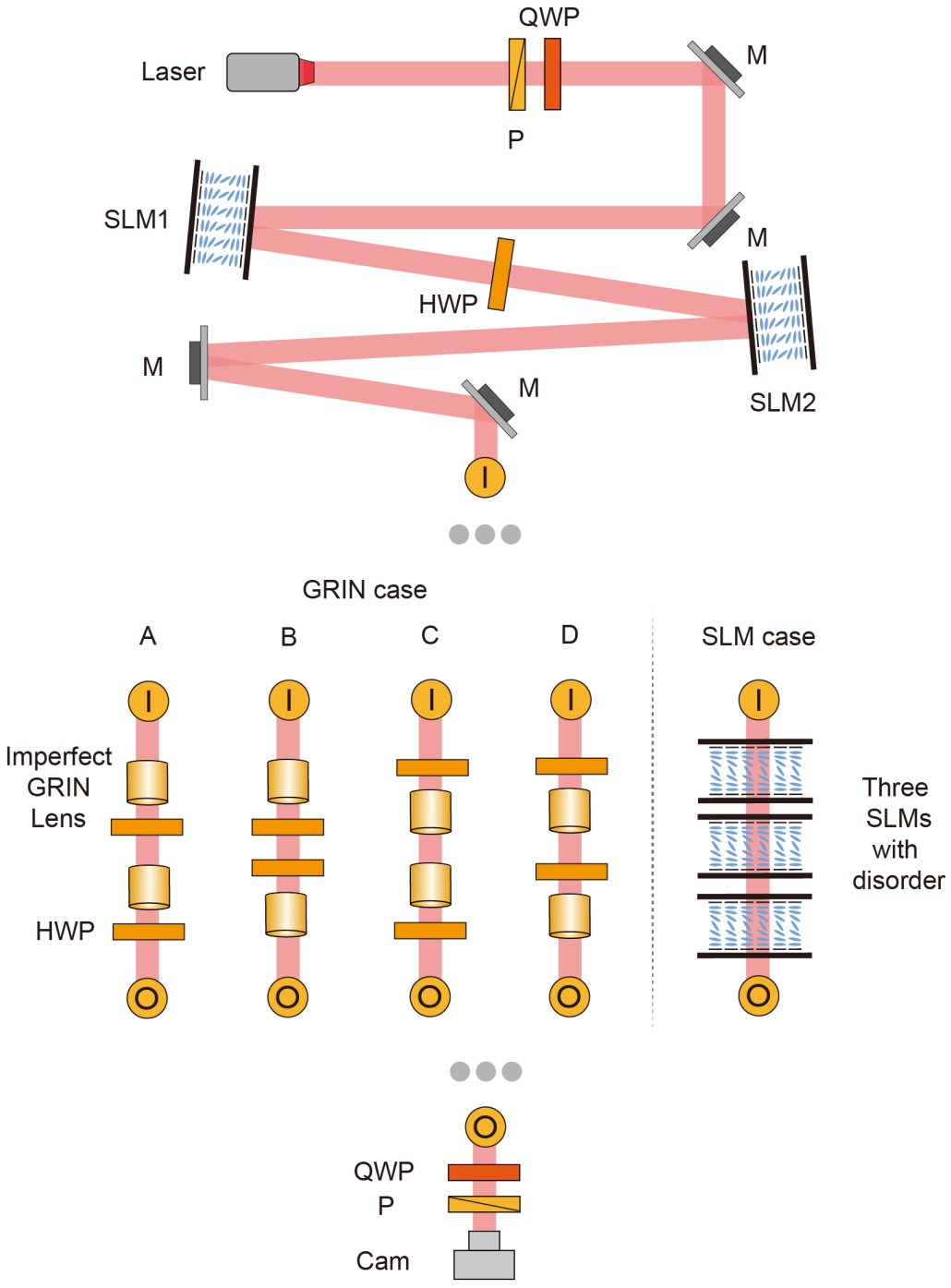

Supplementary Fig. 1: **Experiment assembly.** The complex beam generator and polarimetry configuration adopted in experiments. Components include a He-Ne laser (Melles Griot, 05-LHP-171, 632.8 nm); P: fixed polarizer (Thorlabs, GL10-A); SLM1, SLM2: spatial light modulators (Hamamatsu, X10468-01); HWP: fixed half-wave plate (350-850nm); QWP: rotating quarter-wave plate (Thorlabs, WPQ10M-633); Cam: camera (Thorlabs, DCC3240N). The configurations of the different implementations of the adder used in experiments are also shown. The left (gradient index (GRIN) case) shows the relative placements of modules used to achieve the operations (A) $+2+2$, (B) $+2-2$, (C) $-2+2$, and (D) $-2-2$ while the right (SLM case) shows the 3 SLM cascade used to mimic an adder with disorder.

1.2 Experimental results (gradient index systems)

Supplementary Fig. 2 shows results for the GRIN lens experiment detailed in the main article. Here, skyrmions of orders ranging from -3 to 3 are generated using a cascade of 2 SLMs and passed through the gradient index systems with appropriate waveplates to achieve the operations $+2+2$, $+2-2$, $-2+2$ and $-2-2$. Note from the figure that the numerically computed skyrmion numbers show that our proposed adder efficiently and reliably performs the desired operations. The experiment assembly used is shown in Supplementary Fig. 1.

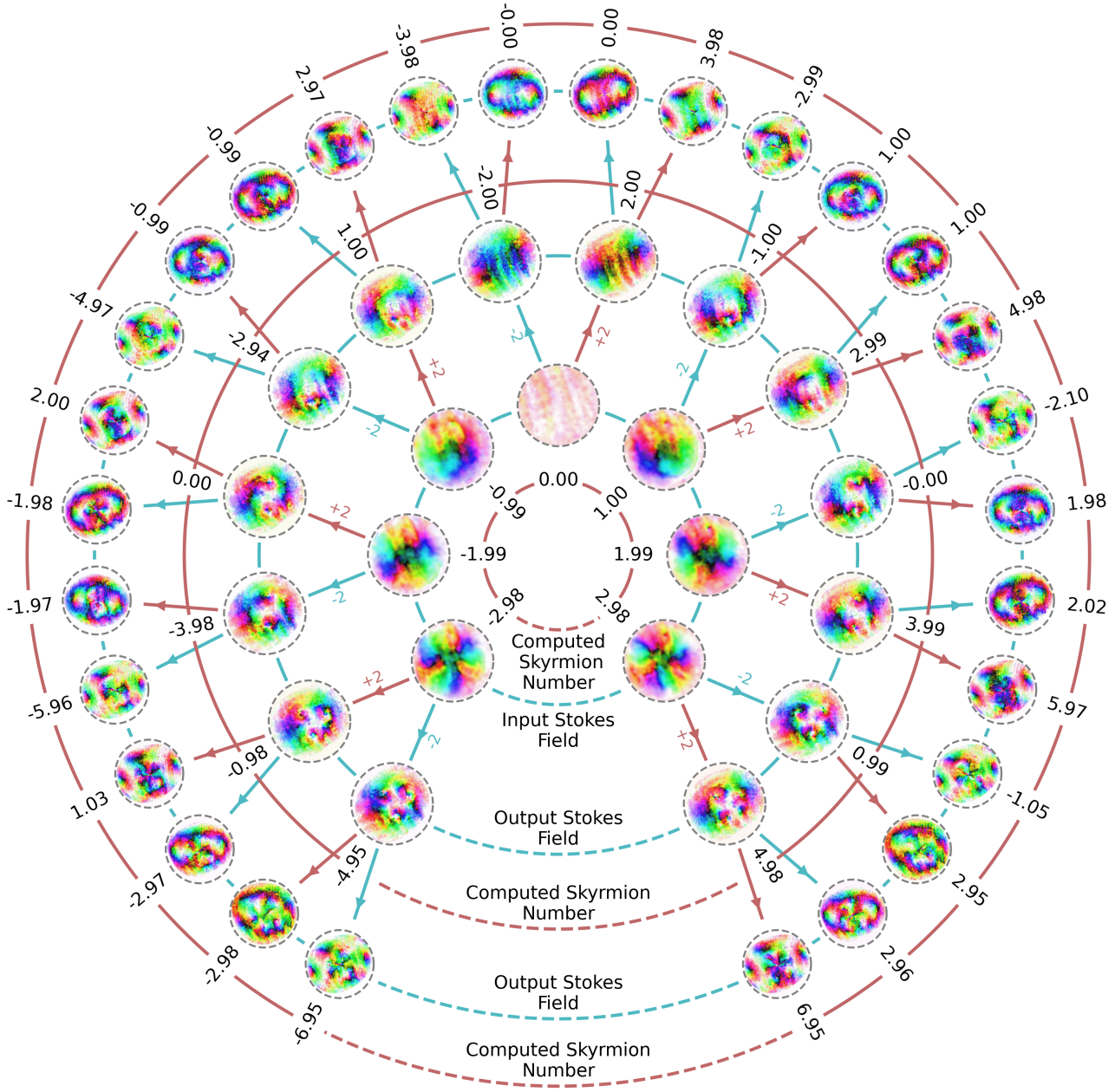

Supplementary Fig. 2: **Experimental results (adders implemented with gradient index systems).** Measured Stokes fields of optical skyrmions passing through adders of order 2 realized using gradient index systems. The innermost ring shows the measured input Stokes fields, the central ring shows the measured fields after a single pass through the medium, and the outermost ring shows the measured fields after a second pass. Here, addition is indicated by red arrows and subtraction by blue ones. Numerically computed skyrmion numbers obtained from measurements are also shown.

The strategy for computing skyrmion numbers from experimental data is adapted from [9], which employs smoothing to enable accurate computation of partial derivatives required for evaluating the skyrmion number integral. We note that smoothing is a homotopy of the field and therefore does not affect its topological charge. The integration domain is determined based on prior knowledge that the output field should be right-circularly polarized (RCP) at its boundary, following these steps: first, consider the array of data points where $s_3 > 0.9$. Using these points, fit a curve of the form $r(\theta)$ via Gaussian process regression. The integration region is then defined as the interior of this curve.

1.3 Experimental results (disordered adder)

In this section, we describe experimental results demonstrating the robustness of our proposed adder to disorder. As explained in the main article, a cascade of 3 SLMs is used to realize the adder and disorder is simulated by introducing random pixel-wise noise to the voltage levels of the SLMs. The noise is added in such a way that it is maximum at the center and gradually decreases to zero at the boundary. As mentioned in the main article, systematic errors due to phase unwrapping lead to lines observed in the output Stokes field, and this can also be considered a form of perturbation. Here we demonstrate the operations $0 + 1$, $0 + 3$, $1 + 1$ and $1 + 3$ at three increasing levels of disorder. The experiment assembly used is shown in Supplementary Fig. 1, and the strategy for computing the skyrmion number is adapted from [9].

Supplementary Fig. 3 shows the full data, with Stokes fields of the different cases presented both using hue plots and polarization ellipses. The computed skyrmion numbers are also shown. The figure is organized such that the lowest disorder case is presented on the left and with increasing disorder moving from left to right. Measured Mueller matrices of the adder at different levels of disorder are also presented.

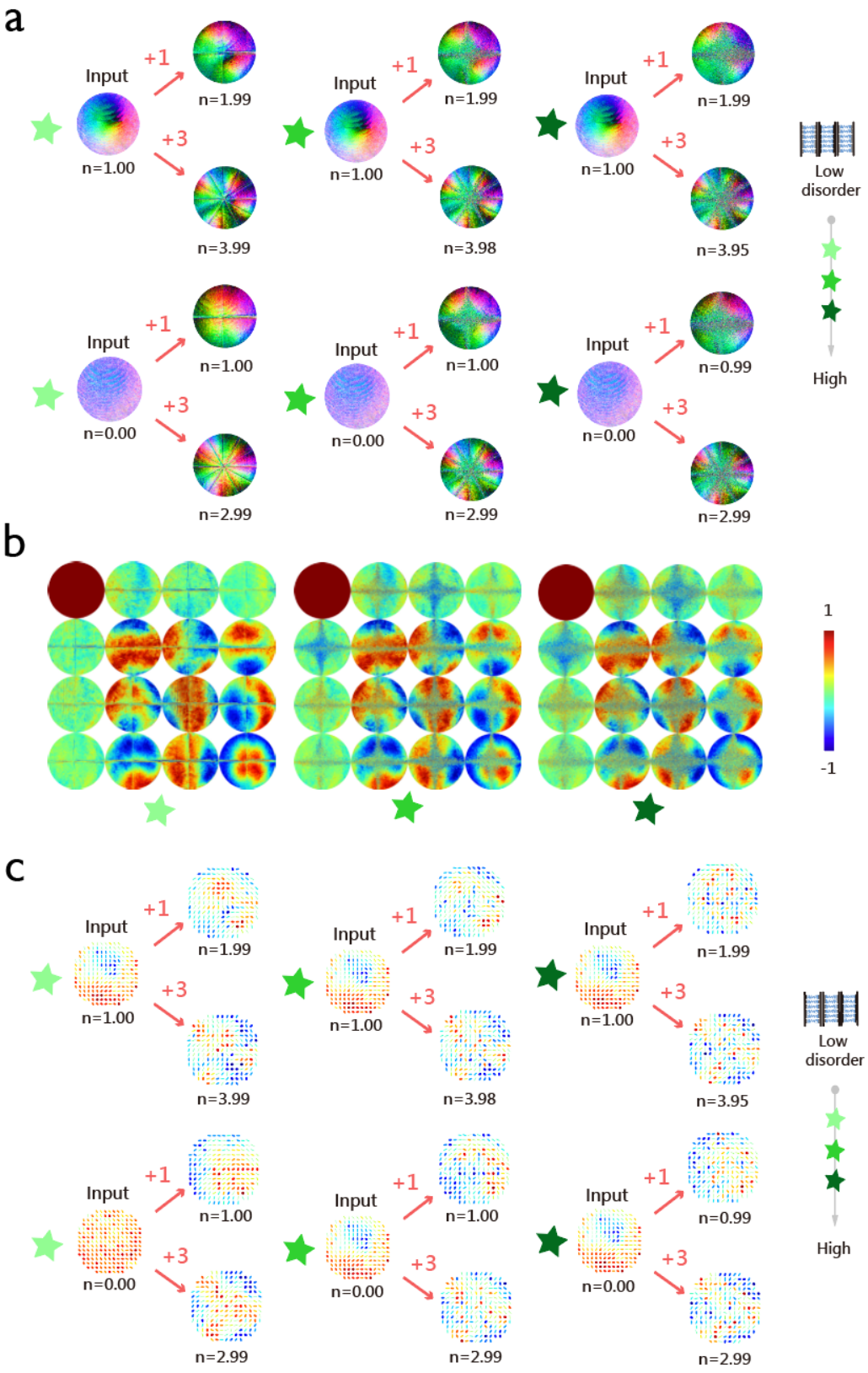

Supplementary Fig. 3: **Experimental results (adders with disorder). a,** Measured Stokes fields and skyrmion numbers of optical skyrmions passing through adders of increasing disorder. **b,** Mueller matrices of the implemented adder at different levels of disorder, increasing from left to right. **c,** Experimental results presented using polarization ellipses.

1.4 Experimental results (disordered generalized adder)

In this section, we describe experimental results demonstrating the robustness of our proposed generalized adder. Here, we show 6 different input boundary SoPs (Supplementary Fig. 4a) passing through adders at three increasing levels of disorder, and whose structure is as described in the main text. The experiment assembly used is shown in Supplementary Fig. 1, and the strategy for computing the generalized skyrmion number is adapted from [10].

The top three datasets in Supplementary Fig. 4 are different SoPs where addition occurs, while the bottom two are different SoPs where subtraction occurs. As mentioned in the main article, this shows that the function of the adder is stable within a range of SoPs, and there is a general robustness to perturbations of the input.

Notice also in Supplementary Fig. 4c that due to disorder, the computed boundary curve (using the methods of [10]) will sometimes self-intersect and form small loops. While theoretically these loops carry a generalized skyrmion number, they depend on the Gaussian process regression used to estimate the field and are artifacts of the computational strategy. However, notice that despite these loops, the generalized skyrmion number of the large components behave as we expect them to. Thus, it is clear that the larger the size of a component, the greater its topological stability. Following [10], in the analysis of our data, we use the area of each connected component to determine when to ignore it and treat loops smaller than a threshold size as errors. Note that the non-linear scaling of the stereographic projection map amplifies the apparent areas of loops near LCP; therefore, the sizes of loops shown in Fig. 4 and Supplementary Fig. 4 do not reflect their true sizes on the Poincaré sphere. This threshold acts as an engineering metric to overcome small loops that arise from measurements in real-world applications. In the future, different optimization strategies can be designed based on specific application conditions or environmental factors.

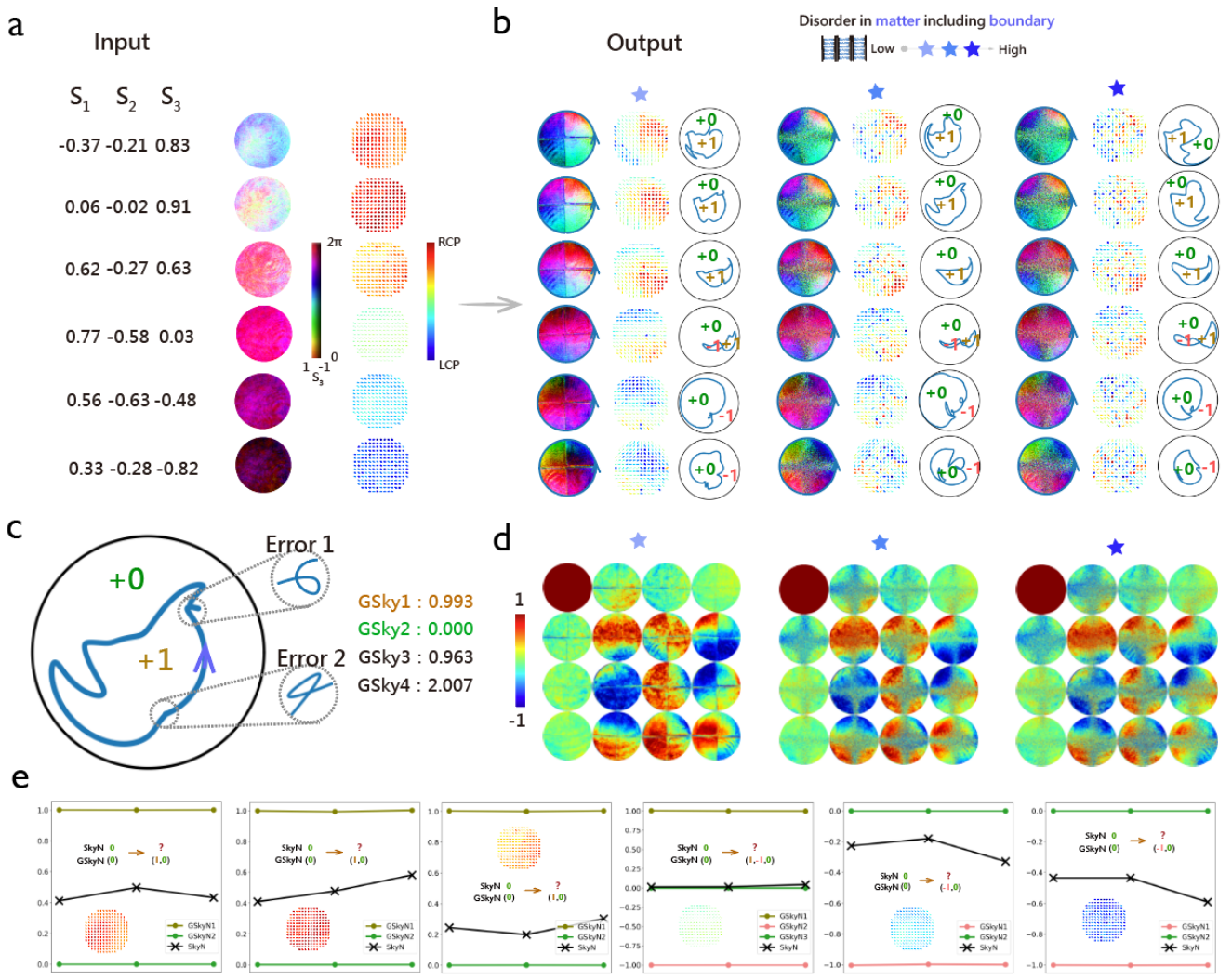

Supplementary Fig. 4: **Experimental results (generalized adders with disorder). a,** Measured input Stokes fields presented using both hue plots and polarization ellipses. The average Stokes parameters are also given. **b,** The output Stokes fields along with the computed stereographically projected boundary curves. The orientation of the different curves follows that shown in Fig. 4 of the main text. The results are presented with the lowest disorder case on the left, and with increasing disorder moving from left to right. The top three rows demonstrate addition, the fourth row demonstrates addition and subtraction simultaneously, and the remaining rows demonstrate subtraction. **c,** A larger version of the stereographically projected boundary curve corresponding to the second input with medium disorder. Notice that disorder can lead to small loops forming when computing the boundary curve, resulting in additional generalized skyrmion numbers. Here, GSky3 is the generalized skyrmion number associated to the loop causing error 1 while GSky4 is the generalized skyrmion number associated to the loop causing error 2. **d,** Mueller matrices of the implemented generalized adder at different levels of disorder, increasing from left to right. **e,** The computed skyrmion number and generalized skyrmion numbers for each input SoP at different levels of disorder. Here, the position of the figures from left to right correspond to the SoPs in **a** from top to bottom.

2 Stability of generalized skyrmions vs ordinary skyrmions

In this paper, we introduced the concept of generalized skyrmions to relax boundary conditions and expand the types of fields that can be used for computations. However, a simpler approach can be taken by using the ordinary skyrmion number for fields with non-integer values. We argue here that the latter approach is less robust. This is because, by construction, the generalized skyrmion number does not take continuous values but rather only values from a discrete set—namely, the set of tuples of integers. This property is what enables the generalized skyrmion number to be stable when the regular skyrmion number is not. That is, since the generalized skyrmion number can only take values in a discrete set, and each value is given by an integral formula (and therefore depends continuously on the field), continuous perturbations of the field cannot change the generalized skyrmion number. Note that this is the same reason why the ordinary skyrmion number is stable provided one can ensure compactification—the boundary condition necessary in ensuring that the skyrmion number integral is integer valued.

However, if compactification does not hold, the skyrmion number becomes unstable as it can now take continuous values, but the generalized skyrmion number is still robust since it remains discrete. For example, consider a typical meron which has polarization field given by

$$S = \begin{pmatrix} \sqrt{1 - f(r)^2}\cos\theta \\ \sqrt{1 - f(r)^2}\sin\theta \\ f(r) \end{pmatrix},$$

where $f(r)$ is some function which runs from $f(0) = 1$ to $f(1) = 0$. Here, the skyrmion number integral evaluates to 0.5. However, notice that if the value of $f(1)$ changes, then so too does the conventional skyrmion number. Therefore, the skyrmion number is not a stable quantity. The generalized skyrmion number, however, remains at $(1, 0)$ for all values $-1 < f(1) < 1$, and is therefore robust to changes in boundary conditions.

Therefore, while it is possible to use non-integer skyrmion numbers for computations, the ordinary skyrmion number in this case is not a topologically robust quantity. It is thus more preferable to use the integer-valued generalized skyrmion numbers instead.

3 Optical skyrmions in the presence of noise

The impact of noise on topology is inherently complex, as noise often involves discontinuous functions, whereas topology relies on continuity to be well-defined. Nonetheless, if we are in a setting where noise can be assumed to be continuous, the theory established in [9] proves that topological protection of the skyrmion number is guaranteed if the perturbation can be achieved by a compactification-preserving homotopy. For arbitrary spatially varying retarders, the only constraint this imposes is that the retarder is uniform on the boundary. Heuristically, this implies that uniform random noise would alter the skyrmion number (since compactification is disrupted), but topological robustness can persist even if the noise is spatially correlated, provided it remains sufficiently small at the boundaries.

Note also that we expect the generalized skyrmion number to exhibit greater topological robustness. In particular, it can tolerate noise at the boundary as long as the noise does not destroy the relevant component under consideration. As demonstrated in the main text, our proposed generalized skyrmion photo-adder remains robust even in the presence of uniform random noise.

For perturbations that are not continuous, the issue becomes more complex. There are two main hurdles that need to be addressed, namely (1) what is largest function space which has a meaningful notion of degree and (2) under what circumstances can we assume that our noisy signal lives in this function space. As it turns out, the degree generalizes to a certain class of distributions, namely functions of vanishing mean oscillation (VMO), and there are Sobolev embeddings $W^{s,p}$ into VMO whenever $sp = n$, $0 < s < n$ for functions on $\mathbb{R}^n$. Note, however, that for $n = 2$, $W^{1,2}$ embeds into VMO but L^2 does not. Since we typically expect uncorrelated random noise to live in L^2, working in VMO may not be quite strong enough to establish the theoretical tolerance of the skyrmion number to random noise.

On top of functional analytic considerations, we also need to address the issue of discretization caused by the finite resolution of the camera. In fact, this may be beneficial given the discussion above: although we may not be able to define the degree on L^2, in the discretized setting, we can view discretization as the camera detecting an "area-averaged," smoothed-out perturbation. The difficulty, however, lies in making sense of continuity and topological numbers in the discrete context. In this regard, there is significant scope to explore further possibilities and deepen our understanding.

4 Skyrmion adder architecture

Here, we describe a possible architecture of an n-bit skyrmion adder that is compatible with wavelength division multiplexing. The 4-bit implementation is shown in Supplementary Fig. 5, and can be easily generalized to higher bits by either increasing the number of generator and adder blocks or the number of wavelengths used. The adder works in the following way:

1. Suppose we want to perform the operation $a + b$. The number a is first converted from electronic signal to optical signal by selectively activating different sources which pass through the required generator block formed from structured matter as described in our main text.

2. The output of the generator block is then channelled simultaneously into the adder block as shown in the figure below, which is converted back into electronic signal via a detector array. As we have described the challenges of detection in our main text, we do not reiterate them here.

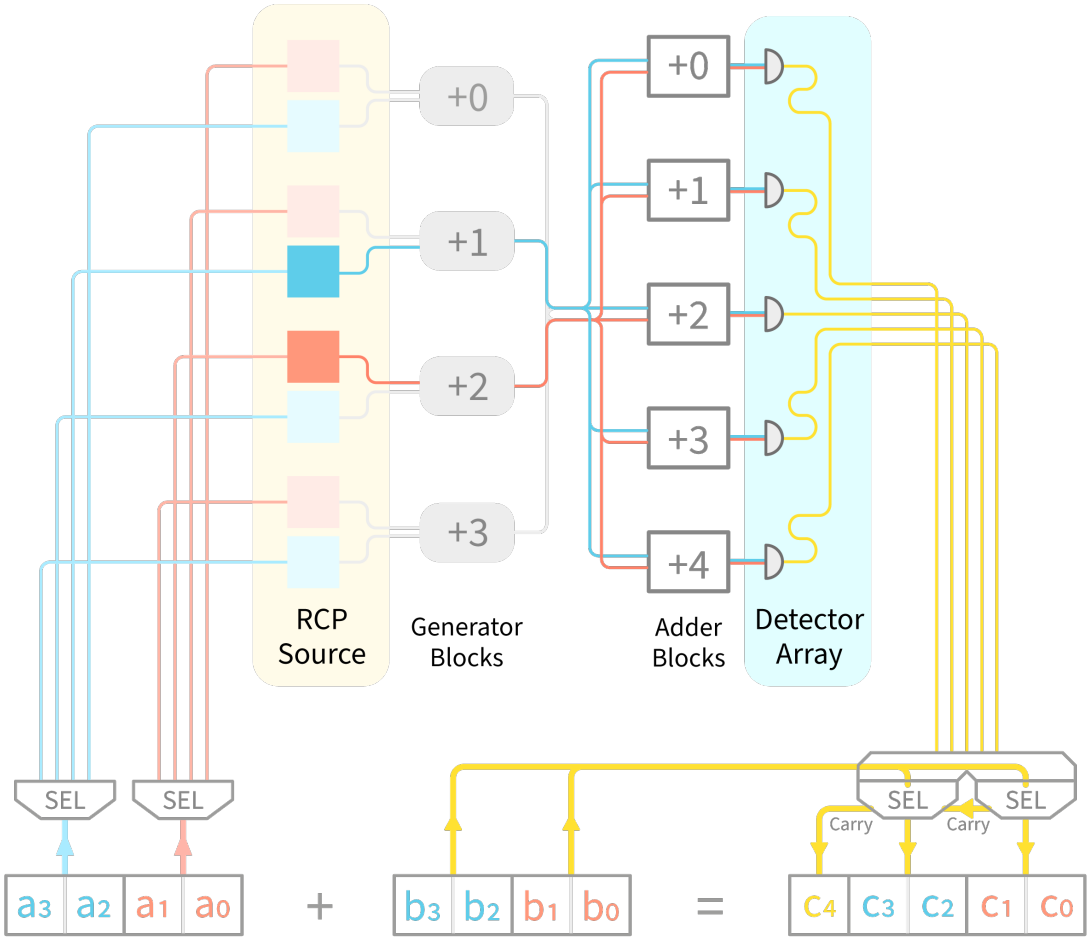

Supplementary Fig. 5: **Possible architecture for an 4-bit skyrmion adder which supports wavelength division multiplexing.** A detailed description of how the adder functions is given in the main text. Here, the gray lines represent waveguides which relay optical signals from one place to another while the yellow lines represent electronic signals. We show two different wavelengths being used at once, represented by the colors red and blue. Note that these colors are intended to distinguish between different independent wavelengths and are not representative of the actual wavelengths of each channel. In practice, comb lasers are a practical approach to generating high-quality beams at different wavelengths, with the wavelengths of the independent channels being closely spaced.

3. The required output from the detector array is then selected using b, with carry logic performed, as of right now, using electronic circuitry.

We note that there is still significant scope for improvement in the architecture presented here, particularly with respect to cascadability. This is an important consideration as analog to digital converters (ADCs) and digital to analog converters (DACs) are some of the most power intensive components in photonic chips today. Therefore, performing as many computations in the optical domain as possible before passing to and from electronic signals is one of the most important design considerations.

Furthermore, as mentioned in the main text, since skyrmions are not constrained by the binary structure of conventional digital electronics, there is potential to explore alternative representations of numbers. For instance, a rational number could be represented by two skyrmions. In this regard, there remains significant room for exploration.

5 Additional Figures

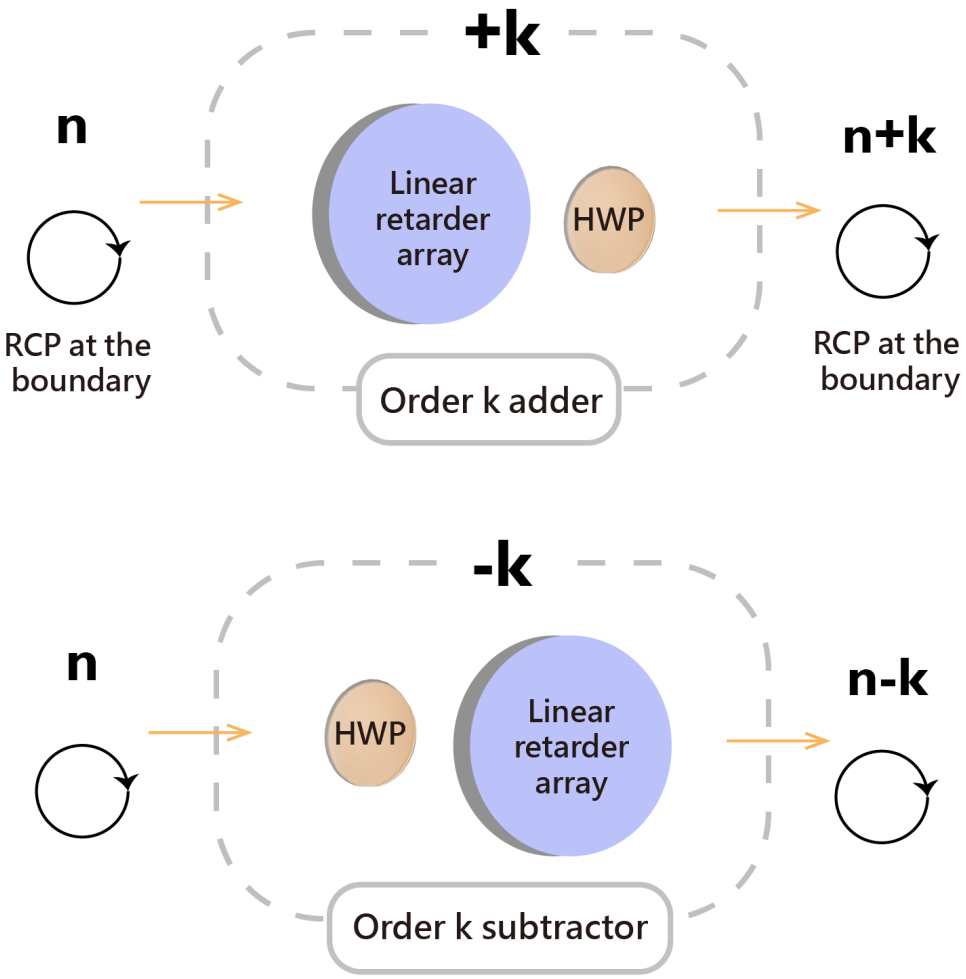

Supplementary Fig. 6: **Adder modules.** The relative placements of half-wave plates (HWP) that enable cascadability of modules designed for inputs that are RCP at the boundary. For addition, the boundary changes from RCP to LCP after passing through the linear retarder array, so a HWP is placed after to restore the boundary back to RCP. For subtraction, the input needs to be LCP at the boundary, so a HWP is place before to adjust the boundary to the correct input polarization state.

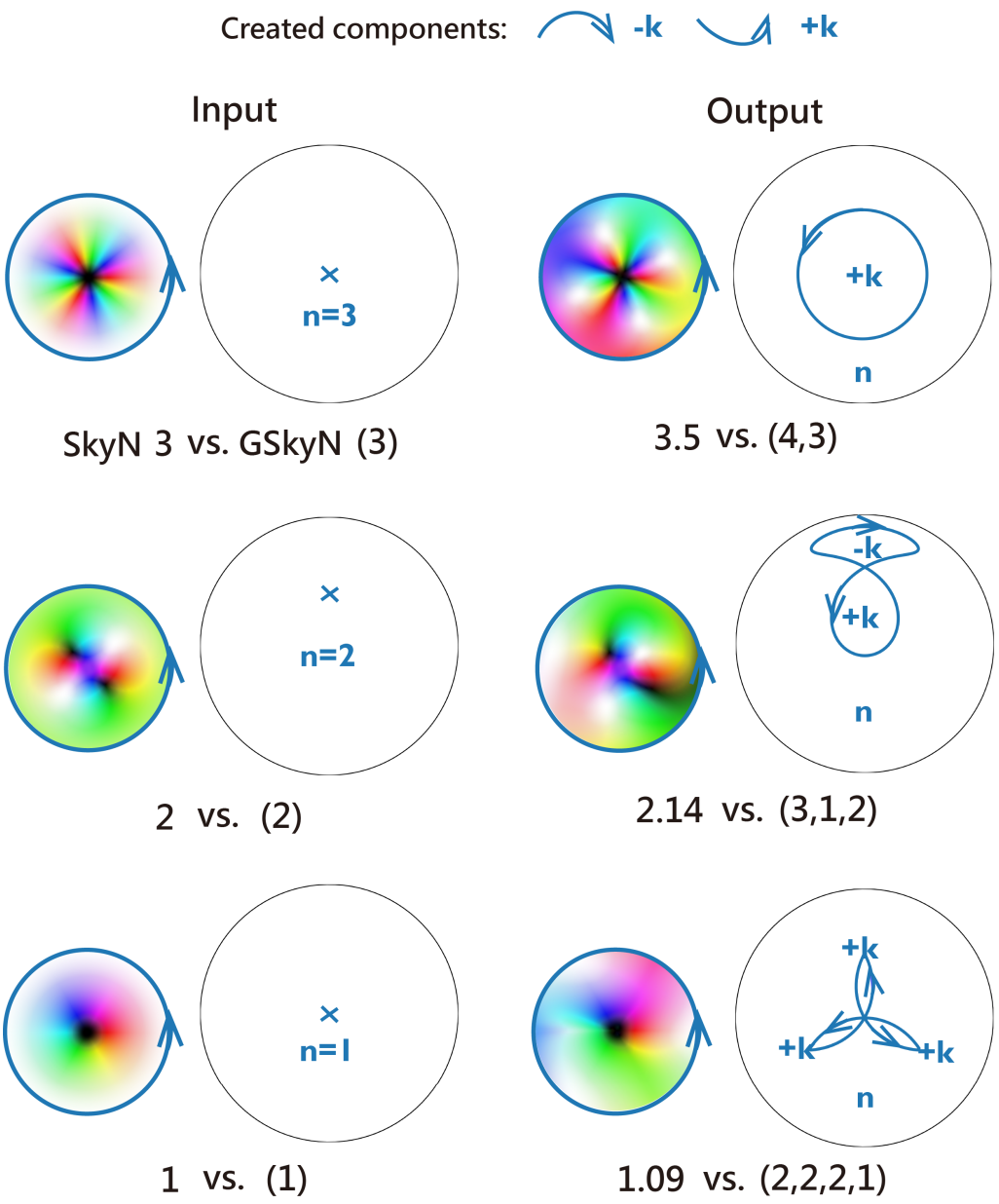

Supplementary Fig. 7: **Generalized skyrmion adders.** As mentioned in the main article, a generalized skyrmion adder works by manipulating the boundary to create new connected components. For each newly created component, the original skyrmion number is increased once for each time the boundary curve encircles the component, accounting for orientation. The figure depicts, from top to bottom, examples of $(n) \mapsto (n+1)$, $(n) \mapsto (n+1, n-1, n)$ and $(n) \mapsto (n+1, n+1, n+1, n)$ adders, where the medium implementing each adder is designed using the strategy presented in Methods 2. Different input and output Stokes fields, along with their stereographically projected boundary curves, are also presented. Finally, the skyrmion number and generalized skyrmion numbers of the various fields are provided.

References

[1] Hu, Q. *et al.* Arbitrary vectorial state conversion using liquid crystal spatial light modulators. *Optics Communications* **459**, 125028 (2020).

[2] He, C. *et al.* A reconfigurable arbitrary retarder array as complex structured matter. *Nature Communications* **16**, 4902 (2025).

[3] Azzam, R. M. A. Stokes-vector and Mueller-matrix polarimetry [Invited]. *Journal of the Optical Society of America A* **33**, 1396–1408 (2016).

[4] Azzam, R. M. A., Elminyawi, I. M. & El-Saba, A. M. General analysis and optimization of the four-detector photopolarimeter. *Journal of the Optical Society of America A* **5**, 681–689 (1988).

[5] Azzam, R. M. A. & Lopez, A. G. Accurate calibration of the four-detector photopolarimeter with imperfect polarizing optical elements. *Journal of the Optical Society of America A* **6**, 1513–1521 (1989).

[6] Azzam, R. M. A. Photopolarimetric measurement of the Mueller matrix by Fourier analysis of a single detected signal. *Optics Letters* **2**, 148–150 (1978).

[7] Smith, M. H. Optimization of a dual-rotating-retarder Mueller matrix polarimeter. *Applied Optics* **41**, 2488–2493 (2002).

[8] Goldstein, D. H. & Chipman, R. A. Error analysis of a mueller matrix polarimeter. *Journal of the Optical Society of America A* **7**, 693–700 (1990).

[9] Wang, A. A. *et al.* Topological protection of optical skyrmions through complex media. *Light: Science & Applications* **13**, 314 (2024).

[10] Wang, A. A. *et al.* Generalized skyrmions. Preprint at `https://arxiv.org/abs/2409.17390` (2024).